Supplementary Information for

Second-order Topological Crystalline Insulator in Metagate-tuned Graphene Surface Plasmons

Minwoo Jung†, Ran Gladstone, and Gennady Shvets

† Email: mj397@cornell.edu

This PDF file includes:

1. Topological Invariants of $\mathcal{C}^6$ Crystalline Insulators
   - $\mathbb{Z}_2$ invariant for an effective low-energy Hamiltonian
   - Topological corner charge
2. Chiral Symmetry Breaking Due to Abrupt Domain Termination
3. Graphene Intrinsic Drude Loss Estimation

Figures S1, S2 and S3

Topological Invariants of $\mathcal{C}^6$ Crystalline Insulators

In this section, we provide more detailed derivations of topological invariants that are relevant to $\mathcal{C}^6$ crystalline insulators. Although the following derivations can be found in many other previous works,[16,26,27,34,37] we still put them here for readers' convenience.

$\mathbb{Z}$ **invariant for an effective low-energy Hamiltonian.** The lowest(1st) and the highest(6th) band in the bulk band structure of $\mathcal{C}^6$ crystalline insulators don't play any essential roles in the physicsof chiral edge state. Also, the important band inversion takes place near point. Thus, let us consider a Hamiltonian that is restricted to the four bands near point. The original 6 by 6 momentum-space Hamiltonian from the tight-binding model in Fig. 2(a) of the main text is

$$\widehat{H}(\mathbf{k})=\begin{bmatrix} 0 & -t_{in} & 0 & -t_{out}e^{-i\mathbf{k}\cdot\mathbf{a}_1} & 0 & -t_{in} \\ -t_{in} & 0 & -t_{in} & 0 & -t_{out}e^{i\mathbf{k}\cdot\mathbf{a}_2} & 0 \\ 0 & -t_{in} & 0 & -t_{in} & 0 & -t_{out}e^{-i\mathbf{k}\cdot\mathbf{a}_3} \\ -t_{out}e^{i\mathbf{k}\cdot\mathbf{a}_1} & 0 & -t_{in} & 0 & -t_{in} & 0 \\ 0 & -t_{out}e^{-i\mathbf{k}\cdot\mathbf{a}_2} & 0 & -t_{in} & 0 & -t_{in} \\ -t_{in} & 0 & -t_{out}e^{i\mathbf{k}\cdot\mathbf{a}_3} & 0 & -t_{in} & 0 \end{bmatrix} \tag{S1}$$

, where $\mathbf{a}_1=a(1,0)$, $\mathbf{a}_2=a\left(-\frac{1}{2},\frac{\sqrt{3}}{2}\right)$, $\mathbf{a}_3=a\left(-\frac{1}{2},-\frac{\sqrt{3}}{2}\right)$.

The four eigenstates at $\mathbf{\Gamma}$ point near the band inversion are

$$\begin{cases} |p_+\rangle=\frac{1}{\sqrt{6}}\exp\left(\left[0,\frac{\pi}{3},\frac{2\pi}{3},\pi,\frac{4\pi}{3},\frac{5\pi}{3},2\pi\right]^T\right)\propto+i\frac{\sqrt{3}}{2}|p_1\rangle+\frac{1}{2}|p_2\rangle \\ |p_-\rangle=\frac{1}{\sqrt{6}}\exp\left(\left[2\pi,\frac{5\pi}{3},\frac{4\pi}{3},\pi,\frac{2\pi}{3},\frac{\pi}{3},0\right]^T\right)\propto-i\frac{\sqrt{3}}{2}|p_1\rangle+\frac{1}{2}|p_2\rangle \\ |d_+\rangle=\frac{1}{\sqrt{6}}\exp\left(\left[0,\frac{2\pi}{3},\frac{4\pi}{3},2\pi,\frac{8\pi}{3},\frac{10\pi}{3},4\pi\right]^T\right)\propto+i\frac{\sqrt{3}}{2}|d_1\rangle+\frac{1}{2}|d_2\rangle \\ |d_-\rangle=\frac{1}{\sqrt{6}}\exp\left(\left[4\pi,\frac{10\pi}{3},\frac{8\pi}{3},2\pi,\frac{4\pi}{3},\frac{2\pi}{3},0\right]^T\right)\propto-i\frac{\sqrt{3}}{2}|d_1\rangle+\frac{1}{2}|d_2\rangle \end{cases} \tag{S2}$$

Here, $|p,d_{1,2}\rangle$'s are the dipole-like and quadrupole-like states introduced in the main text. Projecting $\widehat{H}(\mathbf{k})$ onto the subspace spanned by $|p,d_{\pm}\rangle$'s and taking the limit of $\mathbf{k}\to\mathbf{\Gamma}$, we obtain

$$\widehat{H}_{eff}(\mathbf{k})=\hat{P}\widehat{H}(\mathbf{k})\hat{P}=[|p_+\rangle,|d_+\rangle,|p_-\rangle,|d_-\rangle]\begin{bmatrix}H_-(\mathbf{k}) & 0\\ 0 & H_+(\mathbf{k})\end{bmatrix}[|p_+\rangle,|d_+\rangle,|p_-\rangle,|d_-\rangle]^\dagger \tag{S3}$$

, where $\hat{P}=\hat{P}^\dagger=|p_+\rangle\langle p_+|+|d_+\rangle\langle d_+|+|p_-\rangle\langle p_-|+|d_-\rangle\langle d_-|$, and

$$H_\pm(\mathbf{k})=\begin{bmatrix}(t_{out}-t_{in})+\beta k^2 & \frac{\sqrt{3}}{2}t_{in}(\mp k_x-ik_y)\\ \frac{\sqrt{3}}{2}t_{in}(\mp k_x+ik_y) & -(t_{out}-t_{in})-\beta k^2\end{bmatrix},\qquad \beta=-\frac{3t_{in}}{4}\frac{t_{in}+t_{out}}{2t_{in}+t_{out}}<0 \tag{S4}$$

These Hamiltonians have the structure of Dirac Hamiltonian, whose Chern number calculations are straightforward

$$C=C_+-C_-=\frac{1}{2}[\mathrm{sgn}(t_{out}-t_{in})-\mathrm{sgn}\beta]=\begin{cases}0\ (\text{trivial}), & t_{out}<t_{in}\\ 1\ (\text{topological}), & t_{out}>t_{in}\end{cases} \tag{S5}$$

As discussed in the main text, $\mathrm{sgn}(t_{out}-t_{in})$ is translated to $\mathrm{sgn}(r_1-r_2)$ in our metagate-tuned graphene plasmons, thus yielding a topological(trivial) phase when r_1 is greater(smaller) than r_2.

Topological corner charge. Suppose that a Hamiltonian $\widehat{\mathcal{H}}$ of a periodic system respects a certain discrete symmetry $\hat{S}$: $[\widehat{\mathcal{H}}, \hat{S}] = 0$. Here, a discrete symmetry means that the possible eigenvalues for $\hat{S}$ is countable: $\hat{S}|s_i\rangle = s_i|s_i\rangle$ $(i = 1,2, \ldots)$. Then, since the Hamiltonian commutes with $\hat{S}$, we can always make a simultaneous eigenbasis so that every energy eigenstate of $\widehat{\mathcal{H}}$ is an eigenstate of $\hat{S}$. Also, since the Hamiltonian is periodic, we take the Bloch ansatz for the eigenstates:

$$\widehat{\mathcal{H}}|n,\mathbf{k}\rangle = E_{n,\mathbf{k}}|n,\mathbf{k}\rangle, \qquad |n,\mathbf{k}\rangle = \frac{1}{\sqrt{N}}\sum_{\mathbf{R},m} v_{n,m}(\mathbf{k}) e^{i\mathbf{k}\cdot\mathbf{R}} \hat{c}^{\dagger}_{\mathbf{R},m} \tag{S6}$$

, where $\mathbf{R}$ is the lattice site position, $\mathbf{k}$ is a Bloch momentum, n is the band index, m is the sublattice index, and N is the total number of unit cells. Or, in momentum-space representation:

$$\widehat{H}(\mathbf{k})\vec{v}_n(\mathbf{k}) = E_{n,\mathbf{k}}\vec{v}_n(\mathbf{k}), \;\; \widehat{\mathcal{H}} = \sum_{\mathbf{k}} \begin{bmatrix} \hat{c}^{\dagger}_{\mathbf{k},1} & \hat{c}^{\dagger}_{\mathbf{k},2} & \hat{c}^{\dagger}_{\mathbf{k},3} & \ldots \end{bmatrix} \widehat{H}(\mathbf{k}) \begin{bmatrix} \hat{c}_{\mathbf{k},1} \\ \hat{c}_{\mathbf{k},2} \\ \hat{c}_{\mathbf{k},3} \\ \vdots \end{bmatrix}, \qquad \text{where } \hat{c}^{\dagger}_{\mathbf{k},m} = \frac{1}{\sqrt{N}}\sum_{\mathbf{R},m} e^{i\mathbf{k}\cdot\mathbf{R}} \hat{c}^{\dagger}_{\mathbf{R},m} \tag{S7}$$

Here, $\widehat{H}(\mathbf{k})$ is a square matrix of a dimension equal to the number of sublattice, since we are only considering a spin-less case. In this notation, $|n,\mathbf{k}\rangle = \begin{bmatrix} \hat{c}^{\dagger}_{\mathbf{k},1} & \hat{c}^{\dagger}_{\mathbf{k},2} & \hat{c}^{\dagger}_{\mathbf{k},3} & \ldots \end{bmatrix} \cdot \vec{v}_n(\mathbf{k})$. Each of $|n,\mathbf{k}\rangle$ is an eigenstate of $\hat{S}$, as we have constructed a simultaneous eigenbasis; however, in general, there is no guarantee that each of individual $\hat{c}^{\dagger}_{\mathbf{k},m}$ becomes an eigenstate of $\hat{S}$. As an illustration, let's now come back to a specific example, which is our $\mathcal{C}^6$ crystalline insulator. The entire system carries $\mathcal{C}^6$ symmetry. For $\mathbf{k} = \mathbf{M} = \frac{2\pi}{a}\left(0, \frac{1}{\sqrt{3}}\right)$, however, $\mathcal{C}^6\hat{c}^{\dagger}_{\mathbf{M},m}$ is not colinear with $\hat{c}^{\dagger}_{\mathbf{M},m}$ itself, as the relative phase gain $\exp[i\mathbf{M}\cdot(R_{60^\circ}\mathbf{R} - \mathbf{R})]$ is not constant for all $\mathbf{R}$. For example, this relative phase gain is 1 for $\mathbf{R} = (0,0)$, whereas it is -1 for $\mathbf{R} = (a,0)$. R_θ is a rotation matrix with an angle θ.

Still, there exists certain set of $\mathbf{k} = \mathbf{k}_{inv}$ values that satisfy $\hat{S}\hat{c}^{\dagger}_{\mathbf{k},m} = \hat{c}^{\dagger}_{\mathbf{k},m}$, and we call them invariant momenta. If $\hat{S}$ is a rotational symmetry, they are called rotational invariant momenta (RIM). For examples, RIM for $\hat{S} = \mathcal{C}^6$ is $\mathbf{\Gamma}$; RIMs for $\hat{S} = \mathcal{C}^3$ are $\mathbf{\Gamma}$ and $\mathbf{K}$; and RIMs for $\hat{S} = \mathcal{C}^2$ are $\mathbf{\Gamma}$ and $\mathbf{M}$. Or, if $\hat{S}$ is a time-reversal symmetry ($\hat{S} = \mathcal{T}$), the corresponding time-reversal invariant momenta (TRIM) are $\mathbf{\Gamma}$, $\mathbf{K}$ and $\mathbf{M}$ (here, we consider $\mathcal{T}$ for simple spin-less case, where $\mathcal{T}$ is conjugation; $\mathcal{T}^2 = \mathrm{I}$). At these invariant momenta, we can calculate the symmetry eigenvalues s_i, by simply looking at $\vec{v}_n(\mathbf{k}_{inv})$ without having to consider how $\hat{c}^{\dagger}_{\mathbf{k},m}$'s transform under $\hat{S}$. And, when we examine this vector $\vec{v}_n(\mathbf{k}_{inv})$ of a dimension equal to the number of sublattice, $\hat{S}$ is treated as if it is acting upon a single unit cell instead upon the entire lattice. Thus, for example, the rotational operators in our $\mathcal{C}^6$ crystalline insulator are reduced to

$$\mathcal{C}^6 = \begin{bmatrix} 0 & 1 & 0 & 0 & 0 & 0 \\ 0 & 0 & 1 & 0 & 0 & 0 \\ 0 & 0 & 0 & 1 & 0 & 0 \\ 0 & 0 & 0 & 0 & 1 & 0 \\ 0 & 0 & 0 & 0 & 0 & 1 \\ 1 & 0 & 0 & 0 & 0 & 0 \end{bmatrix}, \mathcal{C}^3 = \begin{bmatrix} 0 & 0 & 1 & 0 & 0 & 0 \\ 0 & 0 & 0 & 1 & 0 & 0 \\ 0 & 0 & 0 & 0 & 1 & 0 \\ 0 & 0 & 0 & 0 & 0 & 1 \\ 1 & 0 & 0 & 0 & 0 & 0 \\ 0 & 1 & 0 & 0 & 0 & 0 \end{bmatrix}, \mathcal{C}^2 = \begin{bmatrix} 0 & 0 & 0 & 1 & 0 & 0 \\ 0 & 0 & 0 & 0 & 1 & 0 \\ 0 & 0 & 0 & 0 & 0 & 1 \\ 1 & 0 & 0 & 0 & 0 & 0 \\ 0 & 1 & 0 & 0 & 0 & 0 \\ 0 & 0 & 1 & 0 & 0 & 0 \end{bmatrix} \tag{S8}$$

at their respective RIMs.

These handy evaluations of s_i's at invariant momenta provide a convenient way of classifying topological phases. Suppose that there are two invariant momenta $\mathbf{k}_{inv}$ and $\mathbf{k}'_{inv}$, and a singly standing band yield symmetry eigenvalues of s and s' at those momenta. Then, each distinct number pair (s, s') is a candidate for topological phases. Or, at least, we know for sure

that the case with $s = s'$ and another with $s \neq s'$ are distinct in their band topology. Those two cases cannot be adiabatically connected, as the latter one has a discontinuity in symmetry eigenvalues along the line between $\mathbf{k}_{inv}$ and $\mathbf{k}'_{inv}$, unlike the former one.

In order to discuss topological charges upon a certain filling fraction (in other words, up to j-th band), we need to consider all the bands below the bandgap of interest. For example, we define a topological invariant associated with $\mathcal{C}^2$ symmetry as below:

$$[\mathbf{M}] = \#M_1 - \#\Gamma_1^{(2)} \tag{S9}$$

Here, $\#M_1$ is the number of states among $\{\vec{v}_m(\mathbf{M}) \,|\, m = 1\sim j\}$ that satisfy $\mathcal{C}^2\vec{v}_m(\mathbf{M}) = +1 \cdot \vec{v}_m(\mathbf{M})$, and $\#\Gamma_1$ defined similarly for $\mathbf{k} = \mathbf{\Gamma}$. For the chiral-symmetric filling considered in our main text, the number of bands below bandgap is $j = 3$. Carrying out the algebra for the Hamiltonian in Eq. S1, we finally obtain

$$[\mathbf{M}] = \begin{cases} 0 \text{ (trivial)}, & t_{out} < t_{in} \\ 2 \text{ (topological)}, & t_{out} > t_{in} \end{cases} \tag{S10}$$

A similar calculation can be done for $\mathcal{C}^3$ symmetry, $[\mathbf{K}] = \#K_1 - \#\Gamma_1^{(3)}$; however, both phases yield a trivial invariant $[\mathbf{K}] = 0$.[34] Thus, for the crystalline insulator described by Eq. S1, $[\mathbf{M}]$ serves as a nontrivial invariant. For the detailed relation between the corner charge and $[\mathbf{M}]$, we simply provide here:[37]

$$Q_c/e = \frac{1}{4}[\mathbf{M}] + \frac{1}{6}[\mathbf{K}] = \begin{cases} 0 \text{ (trivial)}, & t_{out} < t_{in} \\ \frac{1}{2} \text{ (topological)}, & t_{out} > t_{in} \end{cases} \tag{S11}$$

Chiral Symmetry Breaking Due to Abrupt Domain Termination

In this section, we explain why it was necessary to terminate the topological domain with the trivial counterpart, by giving an example that other types of termination fail to produce the topological mid-gap corner states. We show that it is not enough to find any structure that shares the same bandgap position with the topological domain, and that the local chiral symmetry is severely broken at the termination, thereby losing the topological mid-gap corner state.

Figure S1(a) depicts another trivial insulator that also carries $\mathcal{C}^6$ symmetry. This structure, however, has a completely opposite Fermi level landscape, compared to the topological domain; that is, the metagate for this trivial structure has holes right at the effective sublattice site positions described in Fig. 2(a). Thus, the microscopic details of dipolar and quadrupolar basis defined in the topological domain are utterly missing in this new trivial structure. Still, as Fig. S1(b) clearly shows, this structure has a plasmonic bandgap that overlaps with the bandgap of the topological structure. Then, we imbed the topological domain with a hexagonal shape into this new trivial structure, as illustrated in Fig. S1(c).

Then, the embedded structure shows an eigenspectrum provided in Fig. S1(d). At a first glance, this spectrum looks similarly to the results in the main text; however, the corner states obtained by this practice are different from those in the main text. The topological mid-gap corner state in the main text showed its dominant and out-of-phase amplitudes at two effective sublattices that are the second-most close to the corner-most sublattice. On the contrary, this trivial corner state features an in-phase amplitude at two effective sublattices that are the second-most close to the corner-most sublattice, and its dominant amplitude comes from the corner-most sublattice. This mode profile is a signature of a trivial corner state, as reported in a previous work.[34] And, this mode is not guaranteed to be pinned at mid-gap, since there is no symmetry protection. Thus, this trivial mode reacts sensitively to local perturbations on the hopping strengths, whereas the topological mode is not perturbed upon the local perturbations on the hopping strengths

In order to verify this claim that the eigenfrequency of the trivial mode is highly affected by local perturbations on the hopping strengths, we first establish a tight-binding model that represents the system described in Figure S1. We introduce an edge perturbation as depicted in Fig. S2(a), such that the sublattice sites on the edge-most positions (marked as red) are shifted in their on-site potential and the intracell hopping between those red sites is strengthened by δt_{in}. On-site potential Δ_{edge} is to incorporate the fact that the abrupt termination with the structure in Fig. S1(a) decreases mode volume of an effective sublattice at edges, thereby decreasing the plasma energy. The change in the intracell hopping δt_{in} is to incorporate the fact that, since the abrupt termination blocks the wave from dispersing towards the trivial domain, the plasma wave disperses more to the sideways (perpendicular to the edge), thereby increasing the hopping between the sublattices along the edges. Figure S2(b) shows that the eigenspectrum for $\Delta_{edge} = -1.75t$ and $\delta t_{in} = 0.25t$ features trivial corner states as in Fig. S1(d). Also, the mode profile of this tight-binding corner state, as depicted in Fig S2(c), matches well to the mode profile of the plasmonic corner state shown in Fig. S1(e).

Then, we compare how two different types of corner states—one is trivial, and the other of topological origin—react to the variation in δt_{in}. Figure S3 clearly shows that the eigenenergy of the trivial corner states varies a lot as a function of δt_{in}. In other words, this trivial mode is not spectrally pinned at all. On the contrary, the topological corner state is strictly pinned to zero energy, regardless of the strength of the edge perturbation. Therefore, it is crucial to respect the chiral symmetry both in the bulk and at the termination, in order to benefit from chiral-symmetry-protected zero-energy(mid-gap)-pinning.

Graphene Intrinsic Drude Loss Estimation

This section provides a justification that the ultra-low Drude loss assumed in the main text, $\frac{\gamma}{2\pi} = 20\mathrm{GHz}$, is realistically attainable at the state-of-art experimental capabilities. A recent work on cryogenic operation of near-field scanning of graphene plasmons[10] has revealed that, below $T < 100\mathrm{K}$, the dominant mechanism for intrinsic plasmonic loss stems from the electron-phonon scattering in graphene that leads to pseudo-magnetic field (wobbling of Dirac point momentum). Then, the Drude loss is given as:

$$\gamma = \left(1 + \frac{1}{12}\left(\frac{\hbar\omega}{E_F}\right)^2\right)\frac{\beta_A^2 E_F}{\hbar^3 \mu_s v_F^2}\left(\frac{1}{v_l^2} + \frac{1}{v_t^2}\right)k_B T \tag{S12}$$

, where $\beta_A = 5.0\mathrm{eV}$ is the pseudo-magnetic field coupling constant, $\mu_s = 7.6 \times 10^{-8}\mathrm{g/cm^2}$ is the graphene mass density, $v_l = 2.2 \times 10^6\mathrm{cm/s}$ and $v_t = 1.4 \times 10^6\mathrm{cm/s}$ are the velocities of the longitudinal and transversal acoustic phonons in graphene. Assuming $v_F = 1.1 \times 10^8\mathrm{cm/s}$ for the Fermi velocity and $\frac{\omega}{2\pi} = 4\mathrm{THz}$, we obtain:

$$\frac{\gamma}{2\pi} = [1.5 \times (E_F \text{ in eV}) \times (T \text{ in K})]\ \mathrm{GHz} \tag{S13}$$

The recent work mentioned above[10] reported a successful operation of graphene plasmon detection down to $T = 60\mathrm{K}$. For our metagate geometry, at gating $V_g = 1\mathrm{V}$, the Fermi level ranges $E_F = 0.04{\sim}0.16\mathrm{eV}$. Then, according to Eq. S13, the Drude loss in our metagate-tuned graphene would be $\frac{\gamma}{2\pi} = [3.6{\sim}14.4]\ \mathrm{GHz}$. Or, if we assume $T = 90\mathrm{K}$ as in the main text, we get $\frac{\gamma}{2\pi} = [5.4{\sim}21.6]\ \mathrm{GHz}$. It is not clear if this Drude loss estimation would apply locally with varying E_F on graphene; however, even if that is the case, this loss variation is only on the order of $\sim 10\mathrm{GHz}$, which is much less than the bandgap sizes considered in the main text. The bulk bandgap is around $300\mathrm{GHz}$, and even the edge bandgap in Fig. 5(b) is around $100\mathrm{GHz}$. Therefore, we can neglect any non-Hermitian effects from the spatial variation of the loss term. For this reason, we simply took the average value of $\overline{E_F}{\sim}0.15\mathrm{eV}$ over a unit cell, which gave $\frac{\gamma}{2\pi}{\sim}13.5\mathrm{GHz}$ for $T = 60\mathrm{K}$ or $\frac{\gamma}{2\pi}{\sim}20.2\mathrm{GHz}$ for $T = 90\mathrm{K}$, and $\frac{\gamma}{2\pi}{\sim}20\mathrm{GHz}$ was used for the density of state calculation in Fig. 5(b) in the main text. Note that we could have assumed even a 35% lower value.

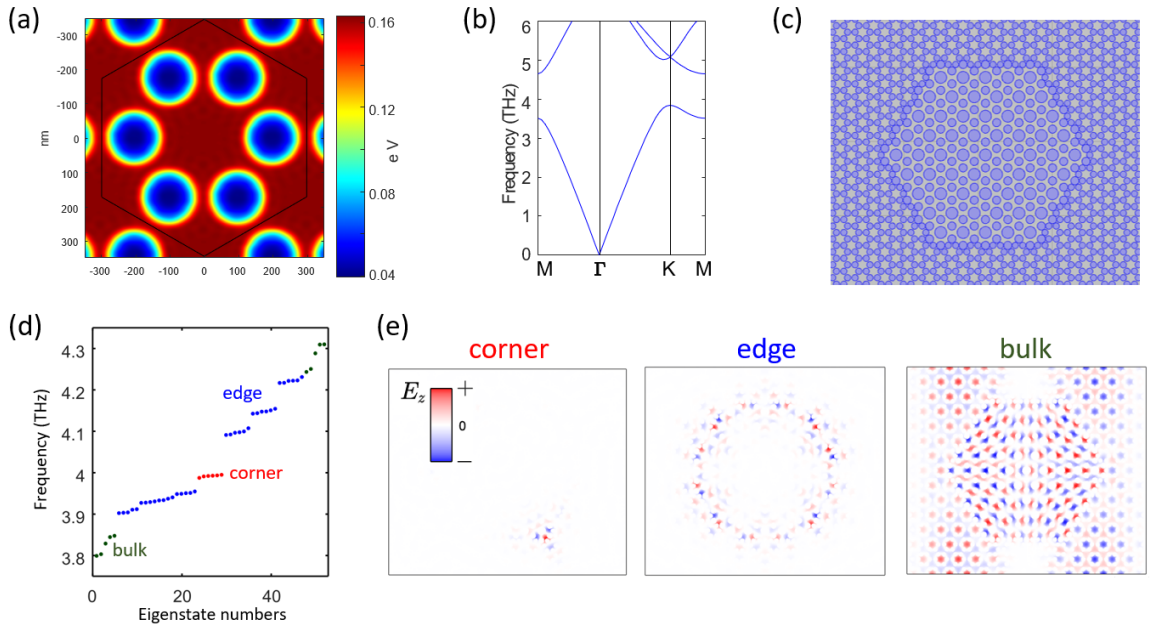

Fig. S1. (a) Fermi level landscape for the new trivial structure with C^6 symmetry; the holes in the metagate are located at the low Fermi energy regions. (b) The corresponding plasmonic band structure. (c) Embedded structure considered for the demonstration of local chiral symmetry breaking; the topological domain is imbedded in the trivial structure. (d) Eigenspectrum from a full electromagnetic frequency domain simulation from COMSOL; the corner, edge, and bulk states are color-coded as red, blue, and dark green dots, respectively. (e) Field profiles of corner, edge and bulk states.

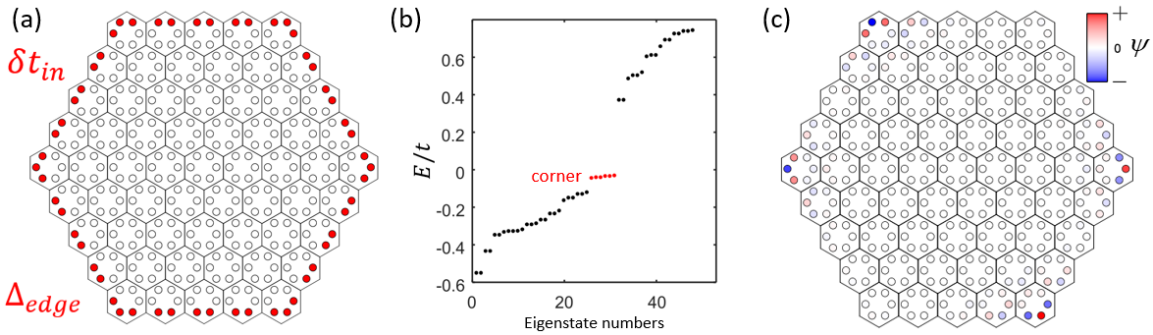

Fig. S2. (a) Tight-binding model setting that corresponds to the system given in Figure S1; we assign on-site potential Δ_{edge} to the sublattices marked as red, and increase the intra-cell hopping strength between red sites by δt_{in}. (b) An eigenspectrum calculated for $t_{in} = 0.875t$, $t_{out} = 1.125t$, $\Delta_{edge} = -1.75t$, and $\delta t_{in} = 0.25t$; the corner states are marked as red. (c) The mode profile of one of the corner states marked in (b).

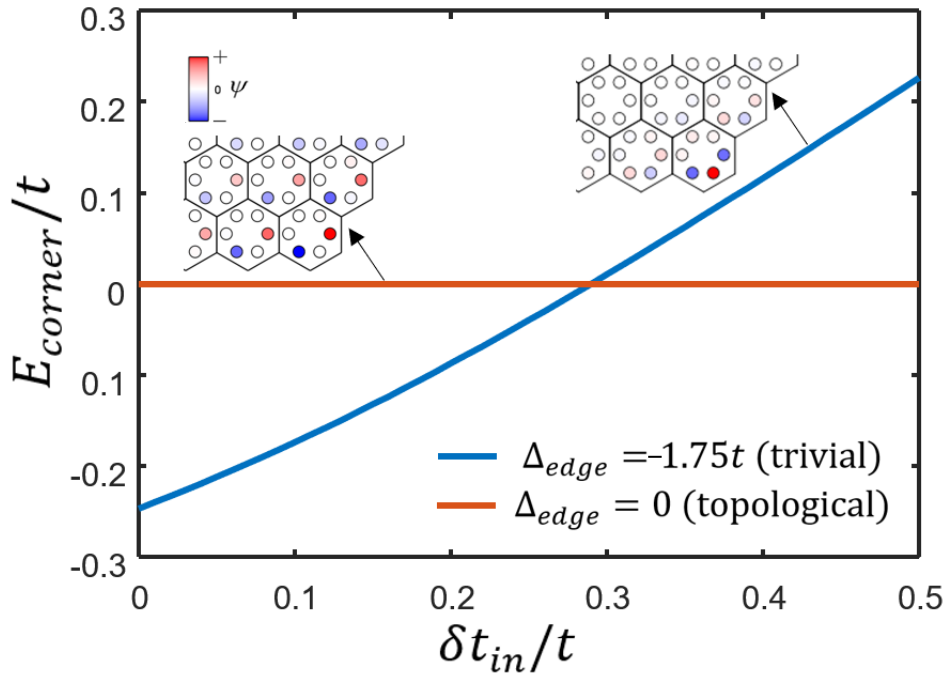

Fig. S3. Comparison between trivial and topological corner states. For each case, the strength of the edge perturbation δt_{in} was varied from 0 to $0.5t$.The topological corner state is strictly pinned at the mid-gap regardless of the strength of hopping perturbation, whereas the eigenenergy of the trivial corner state varies a lot as a function of δt_{in}.